

# RSC Advances



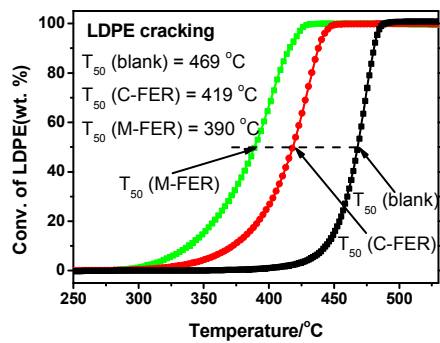
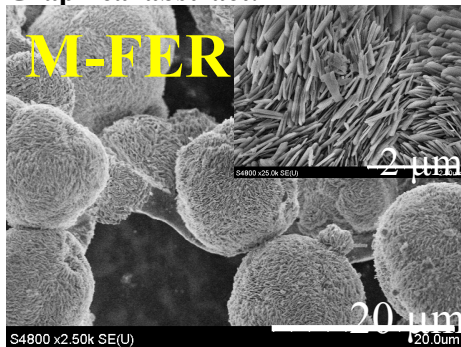
This is an *Accepted Manuscript*, which has been through the Royal Society of Chemistry peer review process and has been accepted for publication.

*Accepted Manuscripts* are published online shortly after acceptance, before technical editing, formatting and proof reading. Using this free service, authors can make their results available to the community, in citable form, before we publish the edited article. This *Accepted Manuscript* will be replaced by the edited, formatted and paginated article as soon as this is available.

You can find more information about *Accepted Manuscripts* in the [Information for Authors](#).

Please note that technical editing may introduce minor changes to the text and/or graphics, which may alter content. The journal's standard [Terms & Conditions](#) and the [Ethical guidelines](#) still apply. In no event shall the Royal Society of Chemistry be held responsible for any errors or omissions in this *Accepted Manuscript* or any consequences arising from the use of any information it contains.

## Graphical abstract:



**Synthesis of Hierarchical Ferrierite Using Piperidine and  
Tetramethylammonium Hydroxide as Cooperative Structure-Directing Agents**

Teng Xue, Huaping Liu, Yi Meng Wang\*

Shanghai Key Laboratory of Green Chemistry and Chemical Processes, Department  
of Chemistry, East China Normal University, North Zhongshan Rd. 3663, Shanghai  
200062, China; Tel: 0086-21-62232251; Fax: 0086-21-62232251; E-mail:  
ymwang@chem.ecnu.edu.cn

Abstract: Zeolite ferrierite aggregates with hierarchical porosity were synthesized using TMAOH and piperidine as cooperative structure-directing agents (co-SDAs). The effect of the relative amount of TMAOH and piperidine on the crystalline phase, textural properties of the products was investigated. Ferrierite aggregates synthesized herein were in size of *ca.* 10-15  $\mu\text{m}$ , composing of nanosheets with thickness of less than 50 nm. The ferrierite aggregates possessed similar acidity and crystallinity with respect to the bulk ferrierite prepared using only piperidine as SDA, but exhibited more than 3 times higher mesopore surface area. The ferrierite aggregates with hierarchical porosity was found to be more efficient in catalytic LDPE cracking due to improved accessibility of large polymer molecules to the active sites.

Key words: ferrierite, synthesis, hierarchical porosity, catalytic performance

## Introduction

Zeolites, a class of microporous crystalline aluminosilicate materials, are widely used in many industrial applications related to catalysis, adsorption and separation due to their high thermal/hydrothermal stability, strong acidity, well-defined microporosity and shape selectivity.<sup>1-4</sup> Their relatively small micropores are beneficial to the shape selective catalytic reactions; however, they can significantly influence the mass transport of the reactants to and from the active sites located within them, resulting in a poor utilization of the zeolite volume in catalyzed reactions, and limiting the activity, selectivity and lifetime.<sup>5, 6</sup> One way to solve the problem is to shorten the diffusion path length in micropores, on guidance of which, zeolite nanocrystals, nano-zeolite aggregates or ‘ultrathin’ zeolites have been successfully synthesized.<sup>7-12</sup>

The zeolite ferrierite framework comprises a bi-dimensional pore network of 10-ring channels ( $0.43 \times 0.55$  nm) running parallel to the c-axis [001] interconnected with 8-ring channels ( $0.35 \times 0.48$  nm) parallel to the b-axis [010]. The intersection of the 8-MR channels and the 6-MR channels in the c-direction leads to spherical cavities (FER cage).<sup>13, 14</sup> Zeolite ferrierite is expected to be a useful material because of its suitability for various industrial applications.<sup>15-18</sup> However, the relatively small size of the pore system in relation to the size of typical substrates can be a restrictive factor to fully exploit its potential in the existing reactions as well as to expand its application to new processes. For example, n-butene isomerization was found to be effectively limited to acidic sites located near the surface of H-FER crystals, and bulk crystals are always filled with slowly diffusing species, such as branched C<sub>8</sub> hydrocarbons and aromatics.<sup>15, 19</sup> Therefore, the introduction of mesoporosity may be

beneficial to reduce diffusion limitations and to fully utilize the active sites in zeolites.

Zeolite ferrierite (FER) with hierarchical porosity can be obtained via the post-synthesis strategy. One way to enhance the accessibility of zeolite ferrierite through the post-synthetic strategy consists in swelling, delaminating and/or pillaring the lamellar PREFER precursor, which could lead to ITQ-6, ITQ-36 and crystalline interlayer-expanded zeolite (IEZ-FER).<sup>20-22</sup> However, this process requires a less conventional template (4-amino-2,2,6,6-tetramethylpiperidine) to synthesize PREFER and an ionic surfactant, cetyltrimethylammonium bromide, as a swelling agent. Perez-Ramirez and co-workers introduced the mesoporosity with combined inter- and intracrystalline nature to the commercial H-ferrierite with the plate-like morphology by selective extraction of silicon in sodium hydroxide solutions.<sup>23</sup> The external surface area of the NaOH-treated ferrierite was nearly  $100 \text{ m}^2 \text{ g}^{-1}$ , increased by a factor of 3-4 with respect to the parent zeolite. The Perez-Ramirez group further investigated a post-synthesis route involving three-step treatment in aqueous  $\text{NaAlO}_2$ , HCl, and NaOH solutions in sequence to generate different hierarchical porous structures from typically microporous ferrierite.<sup>24</sup> The finally obtained sample with intracrystalline mesoporosity showed enhanced transport and catalytic performance during the catalytic pyrolysis of polyethylene. However, post-treatment method usually suffers from the partial damage of zeolitic framework and sometimes the blockage of the micropores by the extra-framework residues generated during the post-treatment and chemical extraction.

Many efforts have been made to synthesize zeolite ferrierite directly with various

morphology and textural properties using different organic molecules as structure-directing agents (SDAs).<sup>25-28</sup> Hong and co-workers reported the synthesis of ferrierite zeolite nano-needles with large interparticle mesoporosity using choline and  $\text{Na}^+$  cations as structure-directing agents. But the composition range yielding pure ferrierite in the presence of choline is quite narrow.<sup>29</sup> Perez-Pariente and co-workers prepared needle-like zeolite ferrierite using tetramethylammonium (TMA) and the bulkier benzylmethylpyrrolidinium (bmp) simultaneously as SDAs.<sup>30, 31</sup> TMA was found to be located inside the ferrierite cage, while bmp was accommodated in the 10-membered ring one-dimensional channels of the FER structure because of its large size. The main drawbacks of these methods lie in the low yield of zeolite or the use of environmental unfriendly reagents such as fluoride.

Herein, we reported the synthesis of zeolite ferrierite aggregates with hierarchical porosity by accelerating the nucleation using  $\text{TMA}^+$  and piperidine as co-SDAs.  $\text{TMA}^+$  cation favors the formation of ferrierite cages and thus enhances the nucleation, and piperidine is supposed to assemble the ferrierite cages to zeolite ferrierite. The effect of molar composition of TMAOH,  $\text{Na}_2\text{O}$ , and piperidine on the crystalline phase and textural properties of the zeolite ferrierite was investigated. Finally, catalytic pyrolysis of LDPE was used as a probe reaction to investigate the catalytic capacity for zeolite ferrierite with hierarchical porosity.

## Experimental

### Zeolite synthesis

Firstly, silica were prepared by adding aqueous HCl solution dropwise to the aqueous solution of  $\text{Na}_2\text{SiO}_3 \cdot 9\text{H}_2\text{O}$ , which was kept stirring until the pH value was lowered to  $\sim 6$ . The freshly precipitated silica was recovered by filtration after being continuously stirred for 2 h. NaOH,  $\text{NaAlO}_2$  (STREM, 54.09% of  $\text{Al}_2\text{O}_3$ , 40.24% of  $\text{Na}_2\text{O}$ ), TMAOH (25% aqueous solution) and piperidine were dissolved in  $\text{H}_2\text{O}$  to obtain a clear solution. The freshly pre-precipitated silica was then added and mixtures with molar composition of  $\text{SiO}_2$ : 0.033  $\text{Al}_2\text{O}_3$ :  $x$  piperidine:  $y$  TMAOH:  $z$   $\text{Na}_2\text{O}$ : 10  $\text{H}_2\text{O}$  ( $x$ ,  $y$ ,  $z$  were shown in Table 1) were obtained. After being stirred for 4 h, the mixtures were then transferred into a Teflon-lined stainless steel autoclave and heated statically under autogenous pressure for the prescribed time at 150 °C. The products were recovered by filtration and washing, dried in air, and calcined at 550 °C for 6 h to remove the templates. The acidic H-form FER was obtained by ion-exchanging the calcined sample in a 1.0 mol  $\text{L}^{-1}$  ammonium chloride solution twice, and then calcinating at 550 °C for 6 h.

### Characterization Methods

The X-ray Diffraction (XRD) patterns of the samples were obtained on Rigaku X-ray diffractometer with nickel filtered  $\text{Cu K}_\alpha$  radiation ( $k = 0.15418$  nm) at 40 kV and 40 mA scanning in the  $2\theta$  scanning range of 5-35 ° at an angular rate of 10 °  $\text{min}^{-1}$ . Relative crystallinity of the products was estimated by measuring the peak area of the characteristic diffraction peaks at  $2\theta = 8.9$  ° and between 22 and 25.5 °, 100% crystallinity being arbitrarily assigned to the sample synthesized with the molar composition of  $\text{SiO}_2$ : 0.033  $\text{Al}_2\text{O}_3$ : 0.35 piperidine: 0.13  $\text{Na}_2\text{O}$ : 10  $\text{H}_2\text{O}$ .

Scanning electron microscopy (SEM) images were obtained on a field-emission scanning microscope model Hitachi S-4800 working under accelerated voltage of 3 KV.

Transmission electron microscopy (TEM) characterization was carried on a FEI TECNAI G2 F30 operating at 300 KV. For the TEM images, the specimens were dispersed in ethanol and placed on holey copper grids.

Nitrogen adsorption-desorption measurements at  $-196\text{ }^{\circ}\text{C}$  were performed in a BELsorp-MAX volumetric adsorption analyzer. The samples were out-gassed at  $300\text{ }^{\circ}\text{C}$  for 6 h before the adsorption measurement. The specific surface area was determined by the BET method using the data points of  $P/P_0$  in the range of about 0.01-0.2. The  $t$ -plot method was used to discriminate between micro- and secondary porosity. Pore size distribution was obtained by the BJH model applied to the adsorption branch of the isotherm.

$\text{NH}_3$ -temperature programmed desorption ( $\text{NH}_3$ -TPD) profiles were obtained on a Tianjin XQ TP5080 autoadsorption apparatus. Hundred milligrams of the obtained H-type ferrierite were pretreated at  $550\text{ }^{\circ}\text{C}$  for 2 h under Helium flow and  $\text{NH}_3$  adsorption was carried out at  $100\text{ }^{\circ}\text{C}$ . The temperature was then raised to  $600\text{ }^{\circ}\text{C}$  at a rate of  $10\text{ }^{\circ}\text{C min}^{-1}$  and the TPD profile for chemisorbed  $\text{NH}_3$  was monitored by a TCD detector.

FTIR measurements were carried out using pyridine as probe molecule to characterize the nature and concentration of acid sites, using a Nicolet Nexus spectrometer equipped with an in-situ vacuum system containing a secondary vacuum. 10-15 mg of

the obtained ferrierite was pressed into self-supporting wafers with a diameter of 11 mm and pre-treated at 600 °C for 2 h (background spectrum). The samples were then cooled down to 50 °C for pyridine adsorption. After that, the samples were subjected to the thermal desorption at 250 °C followed by the IR measurement.

SiO<sub>2</sub>/Al<sub>2</sub>O<sub>3</sub> ratio of the prepared ferrierite zeolites was determined by Thermo IRIS Intrepid II XSP inductively coupled plasma atomic emission spectroscopy (ICP-AES). <sup>29</sup>Si, <sup>27</sup>Al, <sup>13</sup>C solid-state MAS NMR spectra were recorded on a VARIAN VNMRS-400WB spectrometer under one pulse condition. <sup>29</sup>Si NMR spectra were acquired with a 7.5 mm T3HX probe at 79.43 MHz and a spinning rate of 3 kHz. The <sup>27</sup>Al spectra were recorded at a frequency of 104.18 MHz, a spinning rate of 10.0 kHz, and a recycling delay of 4 s. <sup>13</sup>C NMR spectra were recorded with a 7.5 mm T3HX probe at 100.54 MHz and a spinning rate of 5 kHz.

### **Catalytic test**

Catalytic pyrolysis of low-density polyethylene (LDPE) using the obtained acidic H-form ferrierite as catalysts was carried out in a Netzsch STA 449 F3 Jupiter TG-DTA/DSC apparatus. LDPE used in this work was purchased from Alfa Aesar with shape of powder ( $\leq 500 \mu\text{m}$ ), density of  $0.92 \text{ g cm}^{-3}$ , and melting point of 115 °C measured by differential scanning calorimetry (DSC). 3 mg grounded polymer and the 1 mg zeolite powder (25% of the total weight) were carefully weighed, intimately mixed and then loaded in the 30  $\mu\text{L}$   $\alpha\text{-Al}_2\text{O}_3$  crucibles of the thermobalance. The pyrolysis was performed in N<sub>2</sub> ( $70 \text{ cm}^3 \text{ min}^{-1}$ ) from 25 to 800 °C using heating rates of  $10 \text{ }^\circ\text{C min}^{-1}$ .

## Results and discussion

XRD patterns of the samples synthesized with different molar compositions of TMAOH,  $\text{Na}^+$ , and piperidine are shown in Fig. 1. Piperidine was an effective SDA for the synthesis of zeolite ferrierite. Sample a (denoted as C-FER herein for clarity), synthesized without the addition of TMAOH, exhibited typical and well-resolved peaks of zeolite with FER structure, as previously reported.<sup>32,33</sup> This result shows that TMAOH was not indispensable for the formation of zeolite ferrierite. But ferrierite could also be prepared by substituting partial  $\text{Na}^+$  for equivalent moles of  $\text{TMA}^+$ . As shown in Fig. 1, Sample b (denoted as M-FER-1) and Sample c (denoted as M-FER-2), obtained with the molar composition of  $\text{SiO}_2$ : 0.033  $\text{Al}_2\text{O}_3$ : 0.35 piperidine: 0.06 TMAOH: 0.10  $\text{Na}_2\text{O}$ : 10  $\text{H}_2\text{O}$  and  $\text{SiO}_2$ : 0.033  $\text{Al}_2\text{O}_3$ : 0.35 piperidine: 0.10 TMAOH: 0.08  $\text{Na}_2\text{O}$ : 10  $\text{H}_2\text{O}$ , respectively, showed similar XRD patterns to that of Sample a. However, the width of diffraction peaks was much broader, indicating the nanocrystalline properties. Further decreasing the molar ratio of  $\text{Na}_2\text{O}/\text{SiO}_2$  to 0.04 and meanwhile increasing the molar ratio of TMAOH/ $\text{SiO}_2$  up to 0.18, however, led to zeolite Nu-1 with RUT topology (Sample d). If  $\text{Na}^+$  is fully replaced by  $\text{TMA}^+$  when boehmite (64.5% of  $\text{Al}_2\text{O}_3$ ) was used as the aluminum source instead of  $\text{NaAlO}_2$ , the products remained as Nu-1 (Fig. S1). It is reported that more than 17 different structures have been synthesized with  $\text{TMA}^+$  cations as SDA.<sup>30</sup> Whittam *et al* first reported Nu-1 in 1977,<sup>34</sup> where  $\text{TMA}_2\text{O}/(\text{Na}_2\text{O}+\text{TMA}_2\text{O})$  ratio was in the range of 0.05-1.0, especially 0.4-0.7. Herein, The  $\text{TMA}_2\text{O}/(\text{Na}_2\text{O}+\text{TMA}_2\text{O})$  ratio directing to Nu-1 (0.69-1) also fell in the same range of the claim. Compared with Sample c,

Sample e showed an unidentified phase with broad XRD peaks with the ratio of piperidine/SiO<sub>2</sub> decreasing to 0.15, while the ferrierite crystalline phase could be obtained by increasing the piperidine/SiO<sub>2</sub> ratio to 0.60 (Sample f, denoted as M-FER-3). Upon calcination, layer-related [200] diffraction of Sample a shifted to a higher  $2\theta$  region due to the condensation of the interlayer silanols, while that of the other samples remained, suggesting that the nanocrystalline properties and/or the nano-dimension along  $a$  axis were well kept during the calcination. All the obtained ferrierite samples exhibited similar crystallinity, and the SiO<sub>2</sub>/Al<sub>2</sub>O<sub>3</sub> ratio of the products fell in the range of 20-24 (as shown in Table 1) due to the low utilization of silica species in the alkaline systems.

SEM and TEM images of the obtained ferrierite zeolite were shown in Fig. 2. The morphology was greatly influenced by the addition of TMAOH to the synthesis mixtures. C-FER, synthesized without TMAOH, possessed bulk morphology in size of nearly 10  $\mu\text{m}$  (Fig. 2a), where rectangular and platelike crystallites were closely stacked (inset of Fig. 2a). This morphology is most commonly observed in ferrierite crystals.<sup>35,36</sup> When TMAOH was added by replacing partial Na<sub>2</sub>O, spherical ferrierite aggregates formed by individual nano-sized crystallites could be observed. M-FER-1 exhibited aggregated morphologies, as shown in Fig. 2b and Fig. 2e. The size of the aggregates was *ca.* 15  $\mu\text{m}$  and the primary particles forming the aggregates were nanosheets, which were less than 50 nm in thickness, as shown in the high-magnification SEM image in inset of Fig. 2b and high-magnification TEM image in Fig. 2f. The size of ferrierite aggregates decreased when more TMAOH was

used. M-FER-2, prepared by increasing the TMAOH/SiO<sub>2</sub> ratio to 0.10 and decreasing the Na<sub>2</sub>O/SiO<sub>2</sub> ratio to 0.08, possessed the macroscopic aggregates in size of *ca.* 10 μm, where the primary particles were quite thin and more loosely stacked (Fig. 2c). Morphologies seem remained by increasing the amount of piperidine when other conditions remained, as can be observed in Fig. 2b and Fig. 2d. Primary nanosheets of the ferrierite aggregates were loosely stacked, leading to secondary interparticle mesoporosity and macroporosity.

N<sub>2</sub> sorption measurements were performed to characterize the textural properties of the obtained ferrierite zeolite. The isotherms and BJH pore size distributions were shown in Fig. 3 and the summarized data of the textural properties were given in Table 2. C-FER, prepared without the addition of TMAOH, exhibited type I isotherm, which is the characteristics of micropore materials. But samples synthesized with TMAOH exhibited isotherms of combined characteristics of type I and type II, with steep obvious uptake at relative pressure range of 0.5-1.0, showing the existence of mesopores and macropores among the primary zeolitic nano-particles (Fig. 3a). And thus, the hierarchical ferrierite M-FER-1, M-FER-2, and M-FER-3 synthesized with TMAOH and piperidine as co-SDA possessed much larger secondary pore volume ( $V_{\text{sec}}$ ) and external surface area ( $S_{\text{ext}}$ ) than the conventional C-FER prepared using only piperidine as SDA. The ratios of  $V_{\text{sec}}/V_t$  of M-FER-1, M-FER-2, and M-FER-3 were 2-3 times larger than that of C-FER. Hierarchy factor (HF) proposed by Perez-Ramirez and co-workers was used to classify hierarchically structured materials.<sup>37</sup> The HF was 0.03 for a commercial ferrierite with closely stacked platelets

having a length of 0.3-0.8  $\mu\text{m}$  and a lateral width of 50-150 nm. HF could be increased to 0.08 by treating the parent commercial sample with NaOH to different extent.<sup>23, 37</sup> The hierarchical ferrierite aggregates directly synthesized herein, using TMAOH and piperidine as co-SDAs, exhibited a HF of 0.09, slightly larger than that obtained by desilication of commercial ferrierite in aqueous NaOH solution. Pore size distribution of the hierarchical ferrierite samples was determined by the BJH method from the adsorption branch of the nitrogen isotherms (Fig 3b and 3c). For samples synthesized with TMAOH and piperidine as co-SDAs, widely distributed secondary pores ranged from 5 to 200 nm in Fig. 3b and more pronounced increase of the cumulative pore volume of the hierarchical ferrierite in the diameter range of 5-200 nm (Fig. 3c) could be observed. This could be ascribed to the interparticle mesoporosity and macroporosity among the primary ferrierite nano-sheets. Samples prepared from the post-treatment usually suffered seriously from the weight and crystallinity loss. And correspondingly, the micropore volume ( $V_{\text{mic}}$ ) decreased with the increase of secondary porosity. However, the obtained samples herein, using TMAOH and piperidine as co-SDAs, possessed similar  $V_{\text{mic}}$  of 0.13-0.14  $\text{cm}^3 \text{g}^{-1}$  to that of conventional C-FER prepared with only prepared with only piperidine as SDA. M-FER-2 synthesized with the molar ratio of  $\text{TMAOH}/\text{SiO}_2 = 0.10$  exhibited the lowest  $V_{\text{mic}}$  of 0.10  $\text{cm}^3 \text{g}^{-1}$ . This correlates well with its lowest crystallinity obtained by XRD results.

Acidic properties of the ferrierite samples were characterized by  $\text{NH}_3$ -TPD (Fig. 4) and IR of absorbed pyridine (Fig. 5). As shown in Fig. 4, all the ferrierite samples

showed almost the same  $\text{NH}_3$ -TPD profiles with two desorption peaks centered at 230 °C and 460 °C, corresponding to the weak and medium acid of the solid, respectively. The hierarchical ferrierite samples of M-FER-1 and M-FER-3 exhibited the similar amount of weak, medium and total acid with that of the conventional C-FER prepared using only piperidine as SDA (Table 3). While the amount of acid sites of sample M-FER-2 was much lower, this may ascribe to its low crystallinity, as discussed before. The nature of acid (Brønsted acid and Lewis acid) sites can be distinguished by monitoring the IR spectra of adsorbed pyridine. Fig. 5 showed the IR spectra in the region 1600-1400  $\text{cm}^{-1}$ . The strong bands at 1540 and 1454  $\text{cm}^{-1}$  are due to protonation of pyridine molecule by Brønsted acid sites and pyridine adsorbed on Lewis acid sites, respectively. The concentrations of Brønsted and Lewis acid sites were determined using areas of bands at 1540 and 1454  $\text{cm}^{-1}$  and the data were shown in Table 3. The molar extinction coefficient used was 1.67 and 2.22  $\text{cm} \mu\text{mol}^{-1}$  for pyridine interacting with Brønsted and Lewis centers, respectively.<sup>38</sup> The number of Lewis and Brønsted acid sites of sample M-FER-2 was much smaller than the others, which was in accordance with the  $\text{NH}_3$ -TPD results. Furthermore, the amount of Brønsted and Lewis acid of sample C-FER was obviously different with that of the two hierarchical zeolite ferrierite aggregates sample M-FER-1 and sample M-FER-3. The amount of Brønsted acid was slight higher while the amount of Lewis acid was lower for sample C-FER. This might be ascribed to the slightly higher Al content and less defects in the conventional C-FER than that in the two hierarchical zeolite ferrierite aggregates sample M-FER-1 and sample M-FER-3.

Fig. 6 shows the  $^{29}\text{Si}$ ,  $^{27}\text{Al}$ ,  $^{13}\text{C}$  solid-state MAS NMR spectra of the ferrierite samples obtained with TMAOH and piperidine as co-SDAs and or only piperidine as SDA. The resonances at -113 and -107 ppm in the  $^{29}\text{Si}$  MAS NMR spectra, which are assigned to Si(0Al) and Si(1Al) species, could be observed for all the obtained samples. However, the resonance around -100 ppm, which is attributed to silanol or siloxane groups, could only be found in the samples synthesized with TMAOH and piperidine as co-SDAs, indicating the prepared hierarchical zeolite ferrierite aggregates contained abundant silanol groups on the exposed surface.<sup>29, 39</sup> The  $^{27}\text{Al}$  MAS NMR spectra of all the prepared ferrierite samples showed single signals centered at approximately 52 ppm and no resonance around 0 ppm could be observed, showing that the aluminum atoms were tetrahedrally coordinated. The signals at 23, 30, and 44 ppm in the  $^{13}\text{C}$  solid-state MAS NMR spectra, which could be found in all the samples, are assigned to  $\text{CH}_2$  in the piperidine ring. These signals confirmed the integrity of piperidine inside the ferrierite structure. For samples synthesized with TMAOH and piperidine as co-SDAs, an additional signal at 57.3 ppm could be observed. This can be assigned to  $-\text{CH}_3$  groups of the TMA cations trapped in zeolitic cages.<sup>30, 40</sup> These results showed that both TMAOH and piperidine were occluded in the ferrierite framework, suggesting that both molecules may work as SDAs towards the formation of ferrierite aggregates with hierarchical porosity. TMAOH was reported to facilitate the formation of zeolite cavities. For example, zeolite Y (FAU)<sup>41</sup> and ZK-4 (LTA)<sup>42</sup> with sodalite cages and zeolite omega (MAZ)<sup>43</sup> and offretite (OFF)<sup>44</sup> containing gmelinite cages have been obtained using TMAOH as SDA. And

TMAOH was usually located in the cavities of these zeolite frameworks, as evidenced by  $^{13}\text{C}$  CP/MAS NMR.<sup>45</sup> Perez-Pariente and co-workers synthesized zeolite ferrierite, in a fluoride medium, by simultaneous use of tetramethylammonium (TMA) and the bulkier benzylmethylpyrrolidinium (bmp) as SDAs. The  $^{13}\text{C}$  NMR spectrum suggests that TMA is located inside the ferrierite cage. Molecular mechanics calculations revealed the templating role of both cations and confirmed that the most stable configuration of the system corresponds to the siting of TMA within the FER cages, while bmp accommodates in the 10 membered-ring one-dimensional channels. Ferrierite could not be obtained in the absence of TMA, evidencing the important role of TMA during the nucleation of ferrierite in a fluoride medium.<sup>30</sup> Thus herein, we postulate that TMAOH also facilitated the formation of FER cages in the conventional alkali synthetic systems and meanwhile the addition of piperidine further facilitated the assembly of the FER cages to form the hierarchical zeolite ferrierite aggregates.

The interparticle porosity among the primary ferrierite nano-sheets may have a positive influence on the catalytic performance due to the improved accessibility of active sites. Acid-catalyzed LPDE cracking, which was thought to be a suitable probe reaction for diffusion limited reactions due to the nature of the branched polyethylene chain (diameter of 0.494 nm),<sup>46</sup> was used to evaluate the activity of the prepared ferrierite zeolites. Fig. 7a shows the profiles of LDPE conversion versus temperature over the different ferrierite zeolites. Pure LDPE decomposed at very high temperature, but the addition of ferrierite catalyst greatly reduced the decomposing temperatures. More obvious trend can be observed in Fig. 7b, where  $T_{50}$  (temperature for 50%

conversion) is shown versus different catalysts. The uncatalyzed pyrolysis herein shows that 50% of LDPE was decomposed at 470 °C, i.e.  $T_{50} = 470$  °C.  $T_{50}$  was reduced to ca. 420 °C when bulk ferrierite C-FER synthesized without using TMAOH was used as catalyst, which was shifted by ca. 50 °C to lower temperature. Similar trend can be observed in former reports, where a decrease of nearly 40 °C was reported by Perez-Ramirez and co-workers using a commercial ferrierite provided by Zeolyst with Si/Al ratio of 27.<sup>23</sup> The temperature for LDPE degradation was further decreased when hierarchical ferrierite aggregates was introduced as catalyst.  $T_{50}$  was lowered to ca. 390 °C when M-FER-3 was used as catalyst, displaying improved performance compared to the bulk zeolite by about 30 °C. The mesoporous ferrierite obtained by post-treatment enhanced the LDPE degradation performance with respect to the parent zeolite, and a decrease of  $T_{50}$  by 10-60 °C can be observed depending on the desilication conditions.<sup>23</sup> According to this, the zeolite ferrierite aggregates with hierarchical porosity prepared herein exhibited better catalytic performance than bulk zeolite. This improvement of the hierarchical zeolite ferrierite aggregates on the catalytic pyrolysis of LDPE can be attributed to the increased external surface area and amount of exposed acid sites as a consequence of the introduction of secondary interparticle pores. Hierarchical ferrierite aggregates directly synthesized herein showed lower activity in LDPE cracking than mesoporous ferrierite prepared by post-treatment method, although the amount of aluminum was higher. However, the post-treatment was much tedious, which sometimes should experience the NaAlO<sub>2</sub>-treatment, HCl-treatment and NaOH-treatment in sequence.<sup>23, 24</sup> Furthermore,

the distribution of aluminum atoms in zeolite ferrierite framework and external surface, which varied depending on its preparation and post-synthesis modification, may also have an effect on the catalytic performance and need be further investigated.<sup>31, 47, 48</sup>

### Conclusions

In the present study, zeolite ferrierite aggregates with hierarchical porosity were directly synthesized using piperidine and TMAOH as co-SDAs in a conventional alkaline medium. The size of the obtained zeolite ferrierite aggregates was *ca.* 10-15  $\mu\text{m}$  and the primary particles forming the aggregates were nanosheets with the thickness of less than 50 nm. The primary particles were loosely stacked, leading to inter-particle mesoporosity and macroporosity. The hierarchical ferrierite aggregates synthesized herein using piperidine and TMAOH as co-SDAs exhibited more than 3 times higher external surface area with respect to the bulk ferrierite prepared using only piperidine as SDA, while possessing similar acidity and crystallinity. The hierarchical ferrierite aggregates showed more excellent performance with respect to the bulk in the catalytic LDPE cracking due to improved accessibility of the polymer molecules to the active sites.

### Acknowledgments

This work is supported by National Key Technology R&D Program (No. 2012BAE05B02), National Science Foundation of China (No. 21403070, 20890124),

Shanghai Leading Academic Discipline Project (Project B409). And Prof. Wang thanks for the Program for New Century Excellent Talents in University (NCET-11-0145), Ministry of Education of China.

## References

1. A. Corma, *Chem Rev*, 1995, **95**, 559-614.
2. A. Corma, *Chem Rev*, 1997, **97**, 2373-2420.
3. J. Cejka, G. Centi, J. Perez-Pariente and W. J. Roth, *Catal Today*, 2012, **179**, 2-15.
4. W. Vermeiren and J. P. Gilson, *Top Catal*, 2009, **52**, 1131-1161.
5. K. Egeblad, C. H. Christensen, M. Kustova and C. H. Christensen, *Chem Mater*, 2007, **20**, 946-960.
6. J. Perez-Ramirez, C. H. Christensen, K. Egeblad, C. H. Christensen and J. C. Groen, *Chem Soc Rev*, 2008, **37**, 2530-2542.
7. L. Tosheva and V. P. Valtchev, *Chem Mater*, 2005, **17**, 2494-2513.
8. S. C. Larsen, *J Phys Chem C*, 2007, **111**, 18464-18474.
9. Y. Fang, H. Hu and G. Chen, *Chem Mater*, 2008, **20**, 1670-1672.
10. K. Na, M. Choi and R. Ryoo, *J Mater Chem*, 2009, **19**, 6713.
11. X. Zhang, D. Liu, D. Xu, S. Asahina, K. A. Cychosz, K. V. Agrawal, W. Y. Ai, A. Bhan, H. S. Ai, O. Terasaki, M. Thommes and M. Tsapatsis, *Science*, 2012, **336**, 1684-1687.
12. M. Choi, K. Na, J. Kim, Y. Sakamoto, O. Terasaki and R. Ryoo, *Nature*, 2009, **461**, 246-249.
13. I. S. Kerr, *Nature*, 1966, **210**, 294-295.
14. H. Fjellvag, K. P. Lillerud, P. Norby and K. Sorby, *Zeolites*, 1989, **9**, 152-158.
15. R. J. Pellet, D. G. Casey, H. M. Huang, R. V. Kessler, E. J. Kuhlman, C. L. Oyoung, R. A. Sawicki and J. R. Ugolini, *J Catal*, 1995, **157**, 423-435.
16. P. Meriaudeau, R. Bcaud, L. N. Hung and A. T. Vu, *J Mol Catal A: Chem*, 1996, **110**, L177-L179.
17. R. Bastiani, Y. L. Lam, C. A. Henriques and V. T. Da Silva, *Fuel*, 2013, **107**, 680-687.
18. X. Li, X. Liu, S. Liu, S. Xie, X. Zhu, F. Chen and L. Xu, *RSC Adv*, 2013, **3**, 16549-16557.
19. F. C. Meunier, L. Domokos, K. Seshan and J. A. Lercher, *J Catal*, 2002, **211**, 366-378.
20. A. Corma, U. Diaz, M. E. Domine and V. Fornes, *J Am Chem Soc*, 2000, **122**, 2804-2809.
21. W. J. Roth, *Stud. Surf. Sci. Catal.*, 2007, **168**, 221-239.
22. P. Wu, J. Ruan, L. Wang, L. Wu, Y. Wang, Y. Liu, W. Fan, M. He, O. Terasaki and T. Tatsumi, *J Am Chem Soc*, 2008, **130**, 8178-8187.
23. A. Bonilla, D. Baudouin and J. Perez-Ramirez, *J Catal*, 2009, **265**, 170-180.
24. D. Verboekend, R. Caicedo-Realpe, A. Bonilla, M. Santiago and J. Perez-Ramirez, *Chem Mater*, 2010, **22**, 4679-4689.
25. G. Perego, G. Bellussi, R. Millini, A. Alberti and S. Zannardi, *Microporous Mesoporous Mater*, 2002, **56**, 193-202.
26. H. Jongkind, K. P. Datema, S. Nabuurs, A. Seive and W. H. J. Stork, *Microporous Mater*, 1997, **10**, 149-161.
27. N. R. Forbes and L. V. C. Rees, *Zeolites*, 1995, **15**, 444-451.

28. X. Cheng, J. Wang, J. Guo, H. He and Y. Long, *Microporous Mesoporous Mater*, 2009, **119**, 60-67.
29. Y. Lee, M. B. Park, P. S. Kim, A. L. Vicente, C. Fernandez, I. Nam and S. B. Hong, *ACS Catal*, 2013, **3**, 617-621.
30. A. B. Pinar, L. Gomez-Hortiguera and J. Perez-Pariente, *Chem Mater*, 2007, **19**, 5617-5626.
31. A. B. Pinar, L. Gomez-Hortiguera, L. B. McCusker and J. Perez-Pariente, *Chem Mater*, 2013, **25**, 3654-3661.
32. H. Zhang, Q. Guo, L. Ren, C. Yang, L. Zhu, X. Meng, C. Li and F. Xiao, *J Mater Chem*, 2011, **21**, 9494.
33. G. Guo, Y. Long and Y. Sun, *Chem Commun*, 2000, 1893-1894.
34. V. W. Thomas and Y. Barry, *US Pat.*, 4060590, 1977.
35. A. B. Pinar, P. A. Wright, L. Gomez-Hortiguera and J. Perez-Pariente, *Microporous Mesoporous Mater*, 2010, **129**, 164-172.
36. A. Kuperman, S. Nadimi, S. Oliver, G. A. Ozin, J. M. Garces and M. M. Olken, *Nature*, 1993, **365**, 239-242.
37. J. Perez-Ramirez, D. Verboekend, A. Bonilla and S. Abello, *Adv Funct Mater*, 2009, **19**, 3972-3979.
38. C. A. Emeis, *J Catal*, 1993, **141**, 347-354.
39. P. Wu, J. Ruan, L. Wang, L. Wu, Y. Wang, Y. Liu, W. Fan, M. He, O. Terasaki and T. Tatsumi, *J Am Chem Soc*, 2008, **130**, 8178-8187.
40. W. Fan, S. Shirato, F. Gao, M. Ogura and T. Okubo, *Micropor Mesopor Mater*, 2006, **89**, 227-234.
41. G. Zhu, S. Qiu, J. Yu, Y. Sakamoto, F. Xiao R. Xu and O. Terasaki, *Chem Mater*, 1998, **10**, 1483-1486.
42. G. T. Kerr, *Inorg Chem*, 1966, **5**, 1537-1539.
43. R. Aiello and R. M. Barrer, *J Chem Soc A*, 1970, 1470-1475.
44. T. E. Whyte Jr., E. L. Wu, G. T. Kerr and P. B. Venuto, *J Catal*, 1971, **20**, 88-96.
45. R. H. Jarman and M. T. Melchior, *J Chem Soc, Chem Commun*, 1984, 414-416.
46. J. Agullo, N. Kumar, D. Berenguer, D. Kubicka, A. Marcilla, A. Gómez, T. Salmi and D. Y. Murzin, *Kinet Catal*, 2007, **48**, 535-540.
47. A. Janda and A. T. Bell, *J Am Chem Soc*, 2013, **135**, 19193-19207.
48. P. Sazama, J. Dedecek, V. Gabova, B. Wichterlova, G. Spoto and S. Bordiga, *J Catal*, 2008, **254**, 180-189.

**Tables**

Table 1 Synthesis parameters and properties of the obtained samples

| Sample     | Synthesis parameters <sup>#</sup> |          |          | Phase | FER<br>crystallinity/% | SiO <sub>2</sub> /Al <sub>2</sub> O <sub>3</sub><br>ratio |
|------------|-----------------------------------|----------|----------|-------|------------------------|---|
|            | <i>x</i>                          | <i>y</i> | <i>z</i> |       |                        |   |
| a(C-FER)   | 0.35                              | 0        | 0.13     | FER   | 100                    | 20.9  |
| b(M-FER-1) | 0.35                              | 0.06     | 0.10     | FER   | 103                    | 22.1  |
| c(M-FER-2) | 0.35                              | 0.10     | 0.08     | FER   | 96                     | 19.6  |
| d          | 0.35                              | 0.18     | 0.04     | Nu-1  |                        | 26.3  |
| e          | 0.15                              | 0.10     | 0.08     | U*    |                        | 24.7  |
| f(M-FER-3) | 0.60                              | 0.10     | 0.08     | FER   | 105                    | 23.8  |

<sup>#</sup> Molar composition of SiO<sub>2</sub>: 0.033 Al<sub>2</sub>O<sub>3</sub>: *x* piperidine: *y* TMAOH: *z* Na<sub>2</sub>O: 10 H<sub>2</sub>O was used

\* Unidentified phase

Table 2 Textural properties of the prepared zeolite ferrierite

| Sample  | $S_{\text{BET}}^{\text{a}}/$<br>$\text{m}^2 \text{g}^{-1}$ | $S_{\text{ext}}^{\text{b}}/$<br>$\text{m}^2 \text{g}^{-1}$ | $S_{\text{mic}}^{\text{b}}/$<br>$\text{m}^2 \text{g}^{-1}$ | $V_{\text{t}}/$<br>$\text{cm}^3 \text{g}^{-1}$ | $V_{\text{mic}}^{\text{b}}/$<br>$\text{cm}^3 \text{g}^{-1}$ | $V_{\text{sec}}^{\text{d}}/$<br>$\text{cm}^3 \text{g}^{-1}$ | $(V_{\text{sec}}/V_{\text{t}})/$<br>% | HF <sup>c</sup> |
|---------|--|--|--|--|---|---|---------------------------------------|-----------------|
| C-FER   | 334  | 18   | 316  | 0.19   | 0.14  | 0.05  | 26.3                                  | 0.040           |
| M-FER-1 | 357  | 43   | 314  | 0.32   | 0.14  | 0.18  | 56.2                                  | 0.052           |
| M-FER-2 | 339  | 115  | 224  | 0.44   | 0.10  | 0.34  | 77.3                                  | 0.077           |
| M-FER-3 | 362  | 78   | 284  | 0.30   | 0.13  | 0.17  | 56.7                                  | 0.093           |

<sup>a</sup>, BET surface area calculated using BET method applied to the N<sub>2</sub> isotherm; <sup>b</sup>,  $S_{\text{ext}}$ ,  $S_{\text{mic}}$ , and  $V_{\text{mic}}$ , external surface area, micropore area, and micropore volume, respectively, calculated using *t*-plot method applied to the N<sub>2</sub> isotherm; <sup>c</sup>, total pore volume calculated from the N<sub>2</sub> volume adsorbed at  $p/p_0 = 0.99$ ; <sup>d</sup>, secondary pore volume,  $V_{\text{sec}} = V_{\text{t}} - V_{\text{micro}}$ ; <sup>e</sup>, Hierarchy factor, calculated with the formula of  $S_{\text{ext}}/S_{\text{BET}} \times V_{\text{micro}}/V_{\text{t}}$ .

Table 3 Acid properties of the prepared zeolite ferrierite

| Sample  | Determined from NH <sub>3</sub> -TPD/mmol NH <sub>3</sub> g <sup>-1</sup> zeolite |        |       | Determined from FT-IR of chemisorbed pyridine at 250 °C/mmol g <sup>-1</sup> |       |
|---------|---|--------|-------|--|-------|
|         | weak  | medium | total | Brønsted   | Lewis |
| C-FER   | 0.56  | 0.58   | 1.14  | 0.54   | 0.06  |
| M-FER-1 | 0.56  | 0.60   | 1.16  | 0.42   | 0.13  |
| M-FER-2 | 0.36  | 0.47   | 0.83  | 0.19   | 0.06  |
| M-FER-3 | 0.57  | 0.59   | 1.16  | 0.45   | 0.09  |

### Captions of Figures

Fig. 1 XRD patterns of the samples synthesized with a molar composition of  $\text{SiO}_2$ : 0.033  $\text{Al}_2\text{O}_3$ :  $x$  piperidine:  $y$  TMAOH:  $z$   $\text{Na}_2\text{O}$ : 10  $\text{H}_2\text{O}$ . ( $x, y, z$ ) for Sample a (C-FER), Sample b (M-FER-1), Sample c (M-FER-2), Sample d, Sample e, and Sample f (M-FER-3) were (0.35, 0, 0.13), (0.35, 0.06, 0.10), (0.35, 0.10, 0.08), (0.35, 0.0178, 0.04), (0.15, 0.10, 0.08), and (0.60, 0.10, 0.08), respectively.

Fig. 2 SEM (a, b, c, and d) and TEM (e and f) images of the zeolite ferrierite prepared with different amount of piperidine and TMAOH as structure-directing agents. a, C-FER; b, e and f, M-FER-1; c, M-FER-2 and d, M-FER-3.

Fig. 3  $\text{N}_2$  adsorption-desorption isotherms (a) and BJH pore size distributions (b and c) derived from the adsorption branch of the isotherms of the zeolite ferrierite prepared with different amount of piperidine and TMAOH as structure-directing agents (Isotherms for samples M-FER-1, M-FER-2, and M-FER-3 were offset vertically by 50, 100 and 150  $\text{cm}^3 \text{g}^{-1}$ , respectively).

Fig. 4  $\text{NH}_3$ -TPD curves of the zeolite ferrierite prepared with different amount of piperidine and TMAOH as structure-directing agents.

Fig. 5 FTIR spectra of the zeolite ferrierite prepared with different amount of piperidine and TMAOH as structure-directing agent after pyridine adsorption and

evacuation at 250 °C. B: Brønsted acid sites; L: Lewis acid sites.

Fig. 6  $^{29}\text{Si}$ ,  $^{27}\text{Al}$  and  $^{13}\text{C}$  MAS NMR spectra of the as-synthesized zeolite ferrierite prepared with different amount of piperidine and TMAOH as structure-directing agents.

Fig. 7 LDPE conversion versus temperature (a) and correlation between the catalytic activity ( $T_{50}$ , temperature at 50% conversion) during pyrolysis tests (b) over the obtained H-form ferrierite zeolite. Heating rate = 10 °C min<sup>-1</sup>.

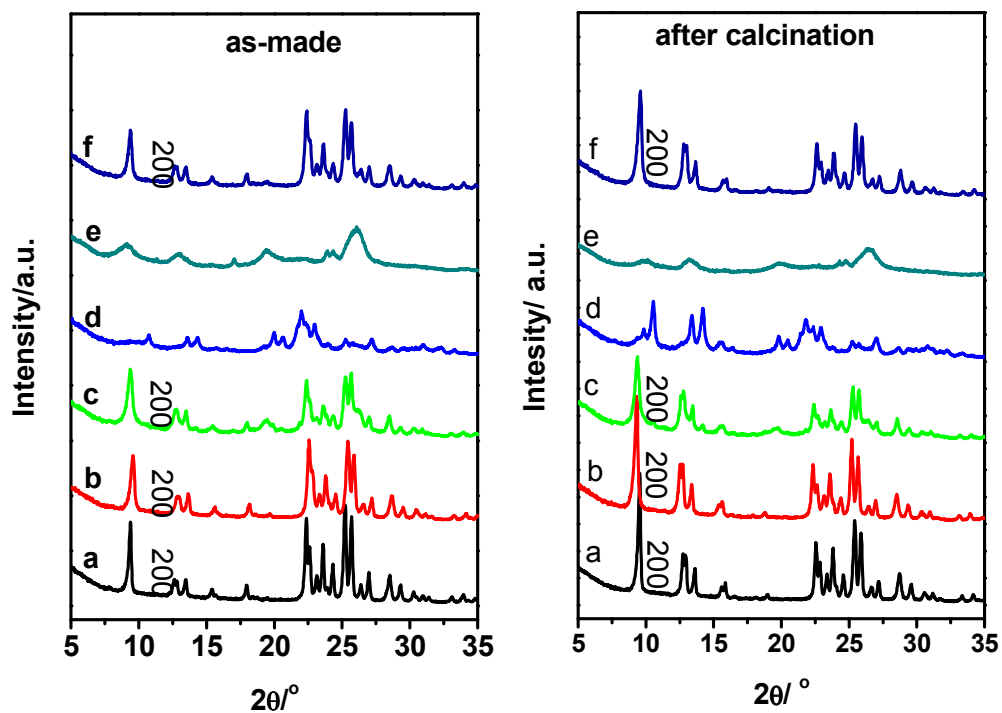


Fig. 1 XRD patterns of the samples synthesized with a molar composition of  $\text{SiO}_2$ :  $0.033 \text{ Al}_2\text{O}_3$ :  $x$  piperidine:  $y$  TMAOH:  $z$   $\text{Na}_2\text{O}$ :  $10 \text{ H}_2\text{O}$ . ( $x, y, z$ ) for Sample a (C-FER), Sample b (M-FER-1), Sample c (M-FER-2), Sample d, Sample e, and Sample f (M-FER-3) were (0.35, 0, 0.13), (0.35, 0.06, 0.10), (0.35, 0.10, 0.08), (0.35, 0.0178, 0.04), (0.15, 0.10, 0.08), and (0.60, 0.10, 0.08), respectively.

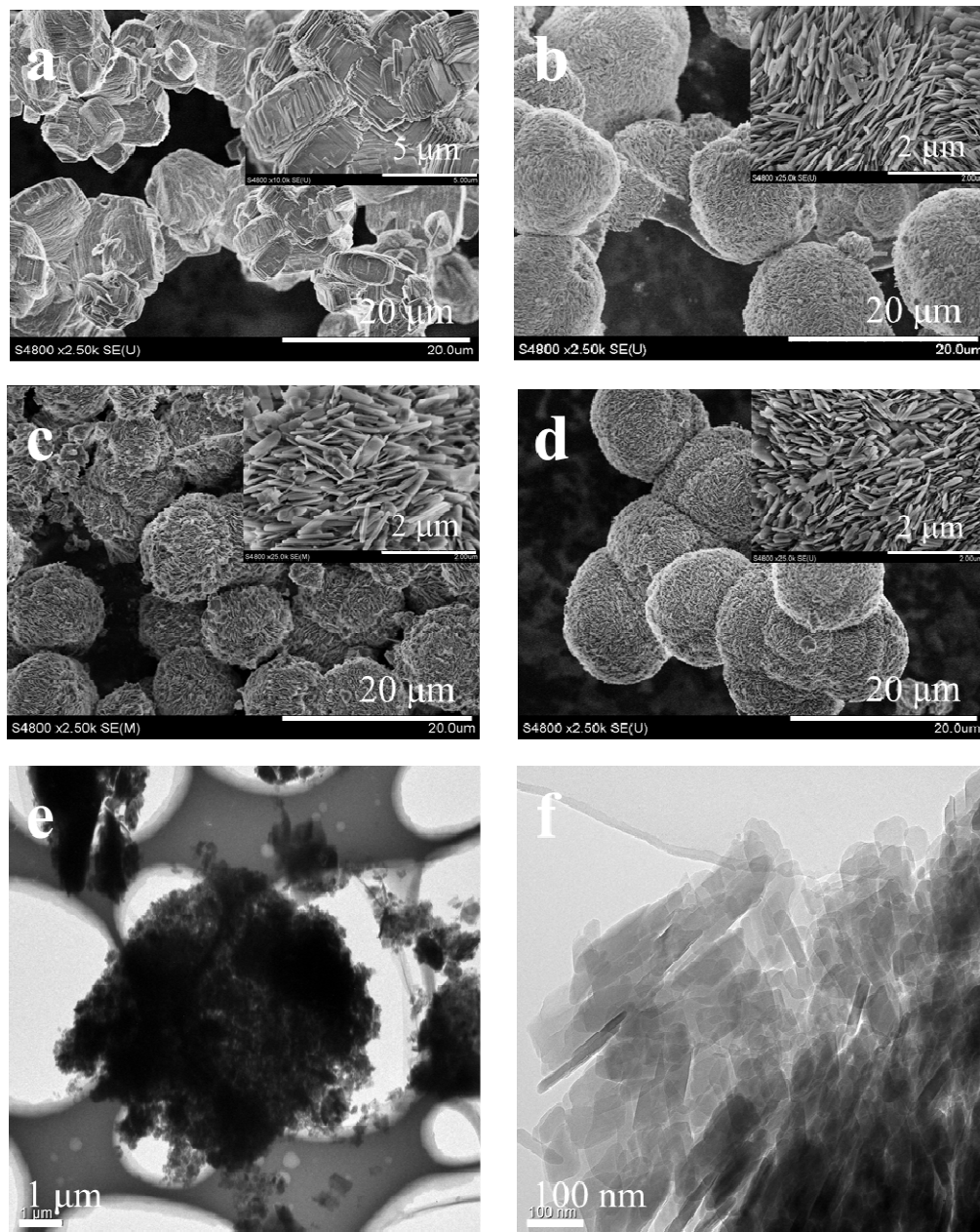


Fig. 2 SEM (a, b, c, and d) and TEM (e and f) images of the zeolite ferrierite prepared with different amount of piperidine and TMAOH as structure-directing agents. a, C-FER; b, e and f, M-FER-1; c, M-FER-2 and d, M-FER-3.

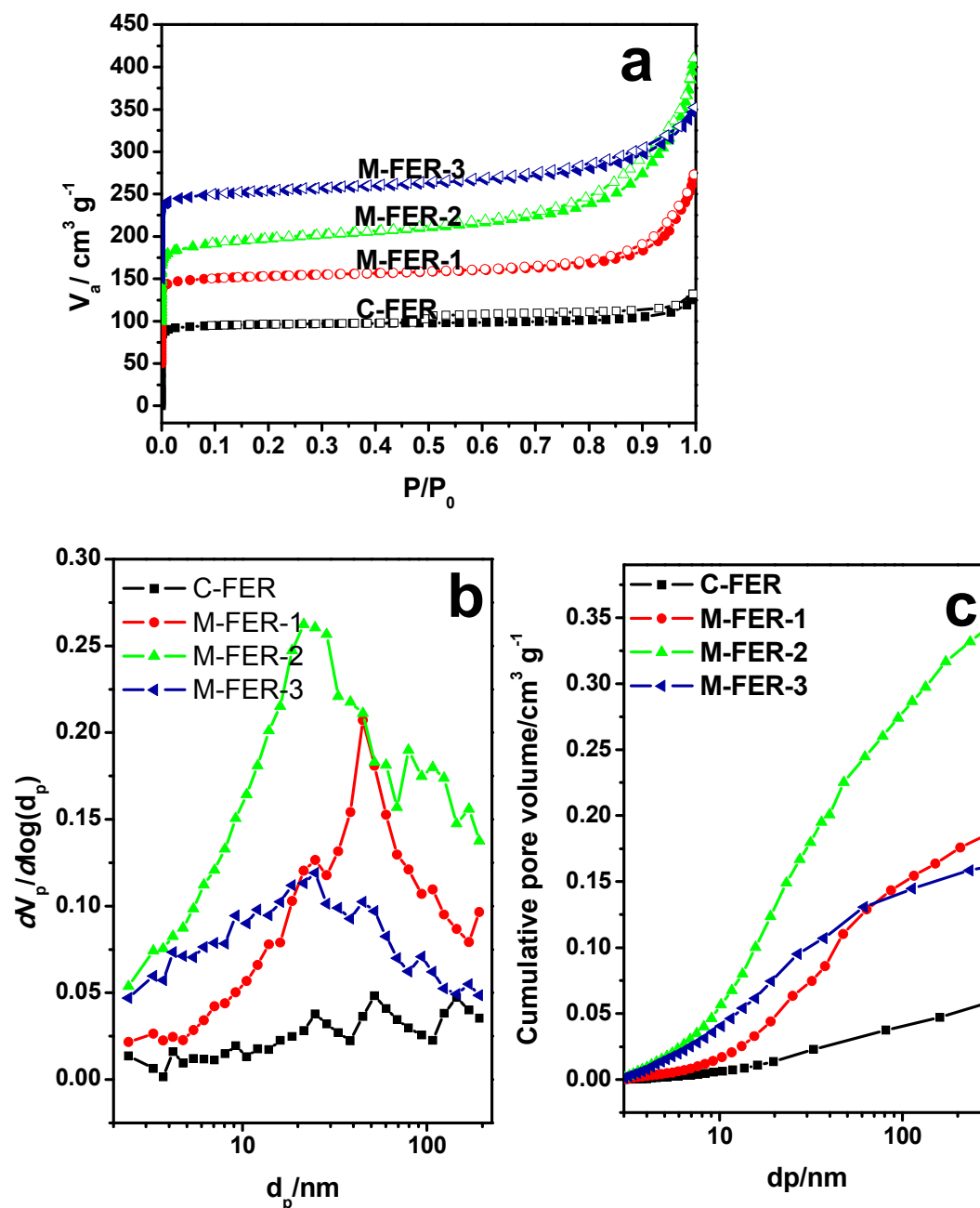


Fig. 3  $\text{N}_2$  adsorption-desorption isotherms (a) and BJH pore size distributions (b and c) derived from the adsorption branch of the isotherms of the zeolite ferrierite prepared with different amount of piperidine and TMAOH as structure-directing agents (Isotherms for samples M-FER-1, M-FER-2, and M-FER-3 were offset vertically by 50, 100 and  $150 \text{ cm}^3 \text{ g}^{-1}$ , respectively).

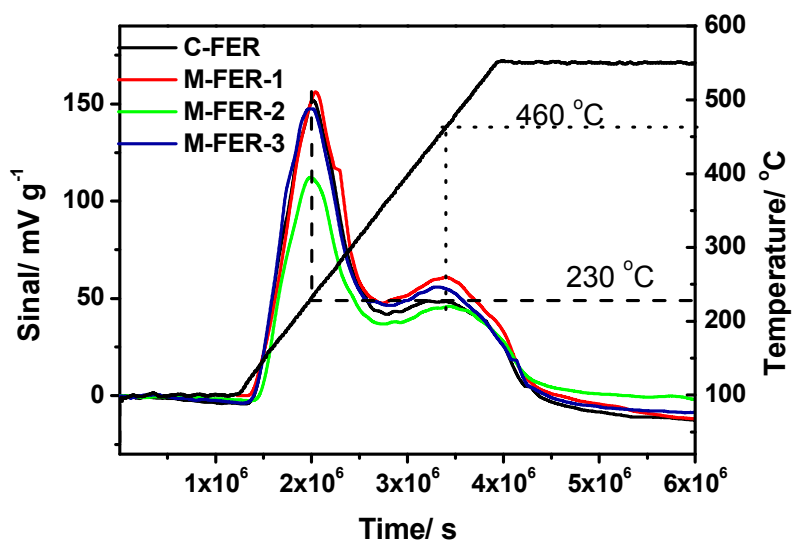


Fig. 4 NH<sub>3</sub>-TPD curves of the zeolite ferrierite prepared with different amount of piperidine and TMAOH as structure-directing agents.

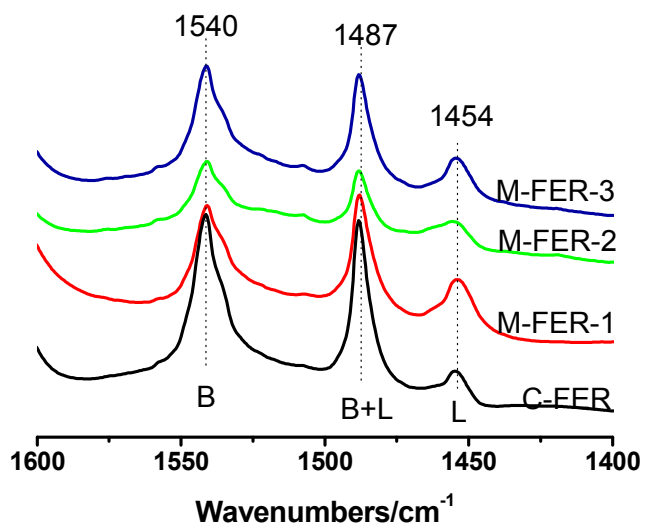
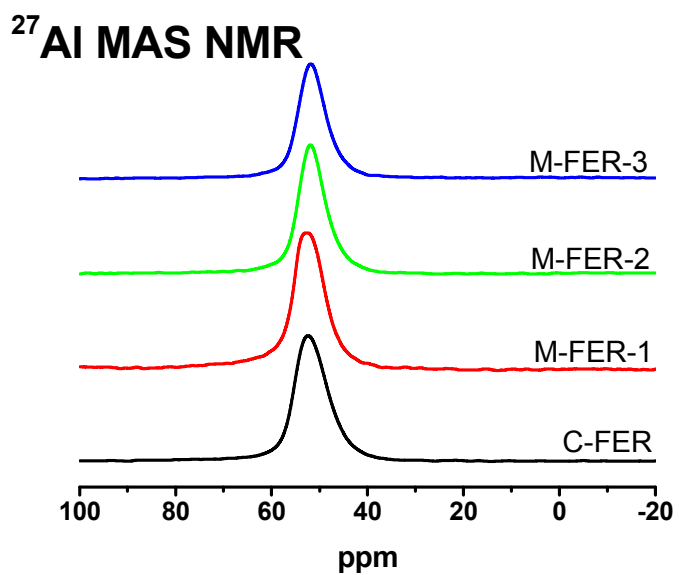
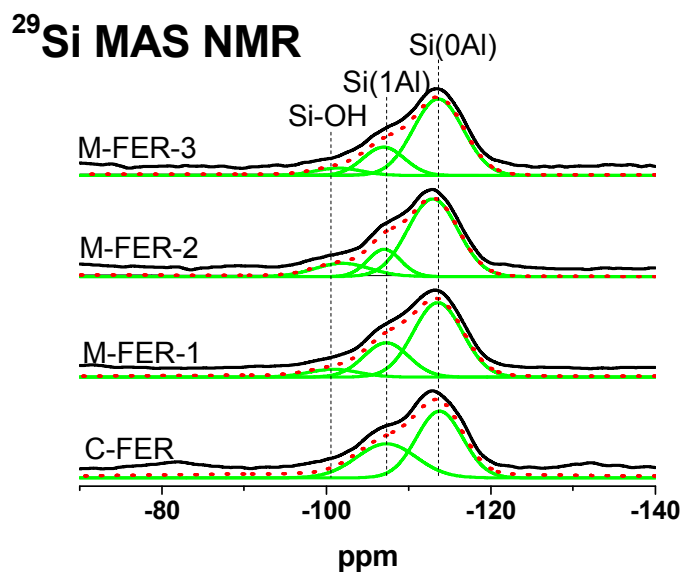


Fig. 5 FTIR spectra of the zeolite ferrierite prepared with different amount of piperidine and TMAOH as structure-directing agent after pyridine adsorption and evacuation at 250 °C. B: Brønsted acid sites; L: Lewis acid sites.



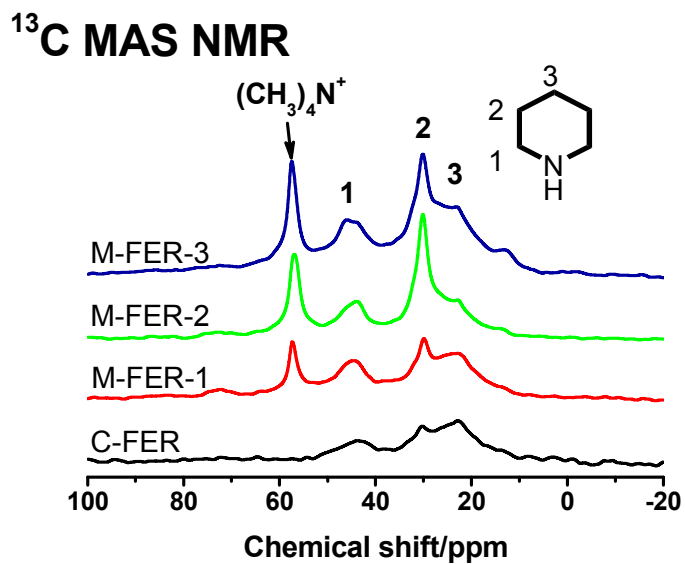


Fig. 6  $^{29}\text{Si}$ ,  $^{27}\text{Al}$  and  $^{13}\text{C}$  MAS NMR spectra of the as-synthesized zeolite ferrierite prepared with different amount of piperidine and TMAOH as structure-directing agents.

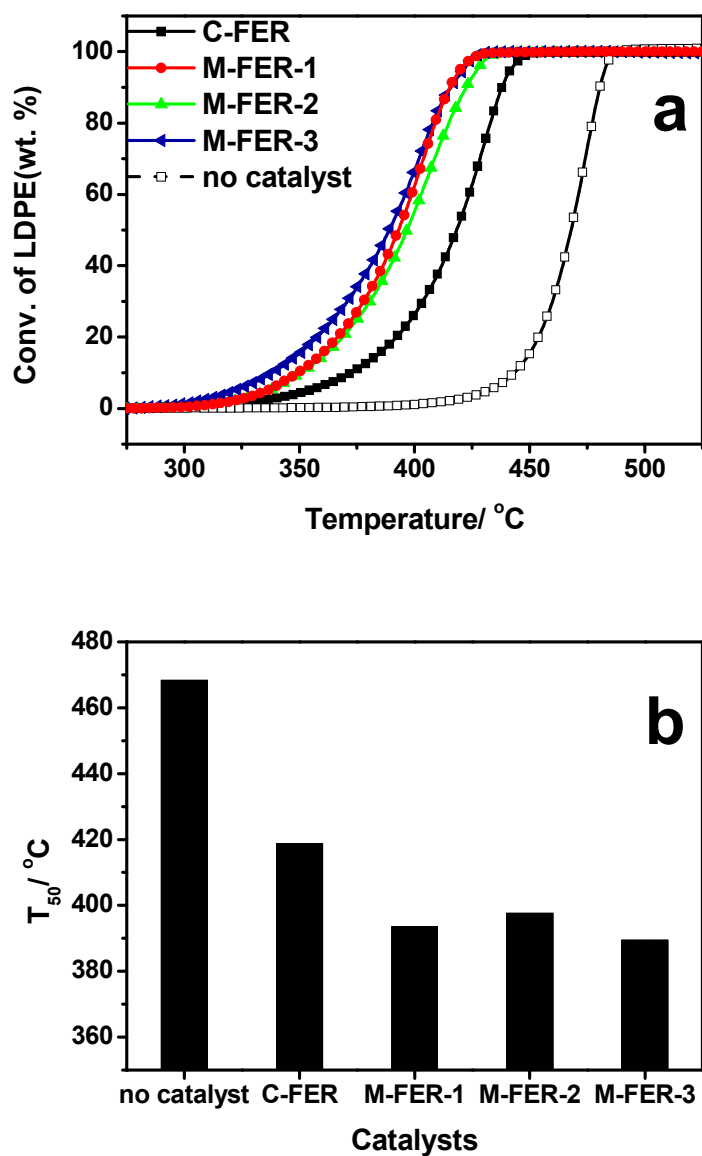


Fig. 7 LDPE conversion versus temperature (a) and correlation between the catalytic activity ( $T_{50}$ , temperature at 50% conversion) during pyrolysis tests (b) over the obtained H-form ferrierite zeolite. Heating rate =  $10\text{ }^{\circ}\text{C min}^{-1}$ .